nanomaterials

MDPI

Article

Strain and Substrate-Induced Electronic Properties of Novel Mixed Anion-Based 2D $ScHX_2$ (X = I/Br) Semiconductors

Ashima Rawat * and Ravindra Pandey

Department of Physics, Michigan Technological University, Houghton, MI 49931, USA; pandey@mtu.edu
* Correspondence: arawat2@mtu.edu

Abstract: Exploration of compounds featuring multiple anions beyond the single-oxide ion, such as oxyhalides and oxyhydrides, offers an avenue for developing materials with the prospect of novel functionality. In this paper, we present the results for a mixed anion layered material, $ScHX_2$ (X: Br, I) based on density functional theory. The result predicted the $ScHX_2$ (X: Br, I) monolayers to be stable and semiconducting. Notably, the electronic and mechanical properties of the $ScHX_2$ monolayers are comparable to well-established 2D materials like graphene and MoS_2, rendering them highly suitable for electronic devices. Additionally, these monolayers exhibit an ability to adjust their band gaps and band edges in response to strain and substrate engineering, thereby influencing their photocatalytic applications.

Keywords: CBM; VBM; heterostructure; band gap

Citation: Rawat, A.; Pandey, R. Strain and Substrate-Induced Electronic Properties of Novel Mixed Anion-Based 2D $ScHX_2$ (X = I/Br) Semiconductors. *Nanomaterials* **2024**, *14*, 1390. https://doi.org/10.3390/nano14171390

Academic Editor: Sotirios Baskoutas

Received: 25 July 2024
Revised: 21 August 2024
Accepted: 21 August 2024
Published: 26 August 2024

1. Introduction

Mixed-anion materials and their 2D counterparts containing more than one anionic species in a single phase have recently attracted significant attention due to their potential to offer novel and attractive functionalities not observed in conventional "single-anion" materials [1]. These materials present exciting opportunities for the development of new properties and applications, expanding the horizons of materials science and technology. By incorporating multiple anionic species, mixed-anion compounds can exhibit unique electronic, structural, and chemical characteristics, paving the way for advancements in energy storage, catalysis, optoelectronics, and other cutting-edge fields. They are synthesized by combining various ionic species, and their appeal lies in the ability to harness disparities in anionic characteristics. These characteristics include ionic radii, charge, electronegativity, and polarizability. By manipulating these anionic attributes, new avenues have been opened for diverse and promising applications of mixed anion compounds. They extend to fields such as visible-light photocatalysts [2–4], ion conductors [5,6], thermoelectrics [7], and superconductors [8]. For instance, these compounds exhibit unique properties that make them highly efficient in harnessing sunlight for various chemical processes, including water splitting and environmental pollutant degradation. In the context of ion conductors, mixed-anion compounds can facilitate the controlled movement of ions, enabling their use in solid-state batteries and fuel cells [1]. Additionally, in the quest for superconductors, these compounds present intriguing possibilities for achieving higher-temperature superconductivity, which could revolutionize energy transmission and storage. The unique properties of mixed-anion compounds, such as their tunable electronic structures and enhanced chemical stabilities, make them promising candidates for the development of next-generation superconductors operating at higher temperatures.

In essence, mixed-anion compounds represent a captivating avenue of exploration in materials chemistry, offering a rich tapestry of opportunities for developing novel materials with exceptional properties. These compounds hold the potential for diverse applications across multiple scientific and technological domains, including energy storage and transmission, catalysis, electronics, and photonics. The continued study and development of

mixed-anion compounds could lead to significant advancements in these fields, paving the way for innovative solutions to some of the most pressing challenges in science and technology today.The scientific research on mixed-anion compounds has primarily been focused on oxide-based compounds, including oxynitrides and oxyfluorides [1]. More recently, oxygen-free mixed-anion compounds like Li_6PS_5Br [9], $Li_{10}GeP_2S_{12}$ [10], CrSBr [11], and $Cs_2PbI_2Cl_2$ [12], have gathered a lot of attention by experimentalists. One significant advantage of these oxygen-free compounds is that the lack of oxygen mitigates electrostatic interactions with conducting ions and reduces migration barriers within the materials.

First principle calculations have become increasingly important in the quest for new 2D materials with novel functionalities and tailored properties. High-throughput computational methods have significantly driven the rapid advancement in this field. Using high-throughput screening on 5619 experimentally known layered 3D compounds, Mounet et al. identified 1036 candidates that could potentially be exfoliated into monolayer 2D materials [13]. Following this pioneering work, numerous other 2D materials have been discovered using the lattice decoration of existing prototypes of 2D materials, further enriching the landscape of 2D materials research and broadening the potential for innovative applications across various technological domains [14–16].

One simpler mixed-anion compound, $LaHBr_2$, was successfully synthesized in 1992 [17], and has also been explored theoretically [18]. By examining the layered structure of $LaHBr_2$, we aimed to identify and investigate similar stable 2D counterparts that can be experimentally synthesized. In this context, we propose a new 2D $ScHX_2$ (X = Br/I) monolayer investigating its structural, mechanical, and electronic properties. The stability of this novel 2D material will be confirmed by employing the density functional theory (DFT) following the three major criteria: lattice dynamical stability, thermodynamic stability, and mechanical stability. This study also involves strain-induced variation in the electronic properties as well as substrate-supported aspects of these mixed anion-based monolayers. Many 2D materials have also been discovered through computational screening based on experimental bulk compounds.

2. Computational Details

The Vienna ab initio simulation package (VASP) was used to perform DFT calculations, based on the projected augmented wave (PAW) pseudo-potential [19–22]. The Perdew-Burke-Ernzerhof form of the generalized gradient approximation (PBE-GGA) [23] has been embraced to describe ion–electron interaction with an energy cut-off set to 500 eV along with the van der Waals (vdW) D3-correction term proposed by Grimme [24]. The convergence criteria for energy and the Hellman-Feynman force acting on each atom were set to 10^{-6} eV and 0.01 eV/Å, respectively. The Brillouin zone was sampled using a Γ centered k-point grid of size (12 × 12 × 1), and periodic image interactions were minimized by using a vacuum of 20 Å along the z-axis direction. The density functional perturbation theory (DFPT) has been used to calculate the phonon frequencies using the PHONOPY package [25–27] in a periodic supercell of 2 × 2 × 1. It is to be noted that the 2D structure of $ScHX_2$ monolayers was derived from the bulk analog of $LaHBr_2$.

3. Results and Discussion

3.1. Ground State Configurations

$ScHX_2$ monolayers belong to the hexagonal symmetry having a space group P6m2 as shown in Figure 1a,c. The simulation box comprises of a hexagonal unit cell with lattice constants a = b and c > 20 Å, and the $\alpha = \beta = 90°, \gamma = 120°$. The lattice consists of 1-Sc, 1-H, and 2-X(Br/I) atoms. The calculated lattice constants and bond lengths are listed in Table 1. The band structures in Figure 1b,d show indirect band gaps of 2.98 eV for $ScHBr_2$ and 2.49 eV for $ScHI_2$.

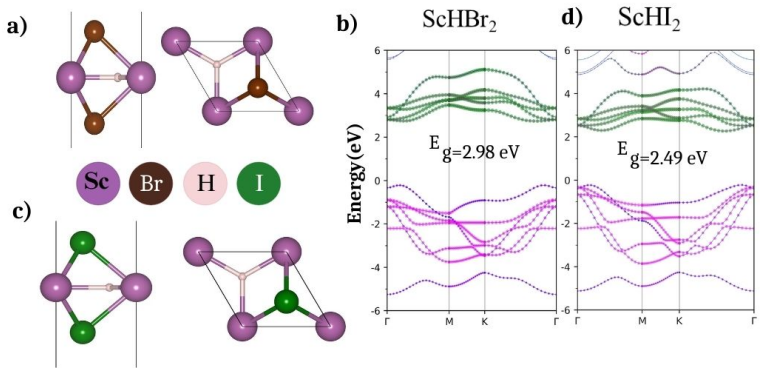

Figure 1. Side and top views of the unit cell and atom−projected band structure of (**a**,**b**) $ScHBr_2$ (**c**,**d**) $ScHI_2$ monolayers (atomic orbitals color code; Sc: green, H: blue and Br/I: pink).

For a better understanding of the nature of bands, we have calculated the atom-decomposed band structures. From Figure 1b,d, we can understand that the valance band maxima (VBM) is dominated by the Br/I atoms with a smaller contribution from H atoms, and the conduction band minima (CBM) is composed mainly of Sc atoms. This has also been confirmed using the band decomposed charge density at the VBM and CBM as depicted in Figure 2. In addition, we have also provided the partial density of states in Figure A1 to observe the above contribution in the Appendix A. The calculated ionization potential (IP), work function (ϕ), and electron affinity (EA) have been listed in Table 1. Note that the IP, ϕ, and EA are crucial properties of semiconductors, especially in the context of their applications in various devices and systems, such as metal-semiconductor junctions, photovoltaic cells, and environmental catalysts. We find that the values of the ϕ, EA, and IP for both monolayers are comparable to the existing 2D materials like graphene, MoS_2, WS_2, phosphorene, etc. [28–30]. In addition the bandgaps are comparable to 2D- $NiPS_3$, γ-CuBr, $GeSe_2$ [31] and higher than that of some of the ferromagnetic 2D materials containing more than two elements ($Mn_2FeC_6N_6$ with E_g = 1.83 eV, $NiRe_2O_8$ with E_g = 1.58 eV) [32].

The effect of spin-orbit coupling (SOC) in both valence and conduction bands is displayed in Figure A2. With the incorporation of SOC, the degeneracy in bands appears though the bandgap remains nearly the same. Hence the SOC effect is not considered in further calculations. Also since the GGA-PBE underestimates the bandgap we have calculated the HSE06 band structures which show a bandgap of 4.02 eV and 3.38 eV for $ScHBr_2$ and $ScHI_2$ monolayer and provided them in Figure A3.

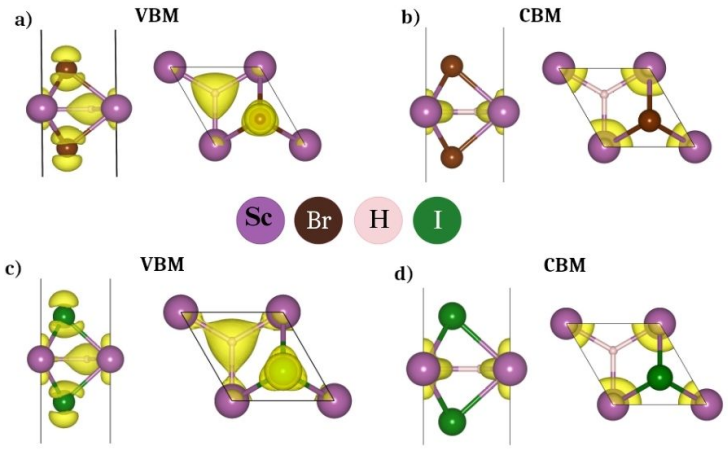

Figure 2. Top and side views of the band decomposed charge density at the valence band maxima (VBM) and conduction band minima (CBM) for (**a**,**b**) $ScHBr_2$ and (**c**,**d**) $ScHI_2$ monolayers at an isosurface value of 0.003 e/Å^3.

Table 1. Calculated Lattice Parameters (a = b), bond-lengths, Sc-H, Sc-Br/I, Ionisation Potential (IP), Work Function (ϕ), and Electron Affinity (EA) in $ScHBr_2$ and $ScHI_2$ monolayers. * Refs. [24,25].

Monolayer	a = b (Å)	Sc-H (Å)	Sc-X (Å)	IP (eV)	ϕ (eV)	EA (eV)
$ScHBr_2$	3.62	2.08	2.78	6.35 6.42 [a] 6.09 [b]	5.99 5.23 [a] 4.61 [c]	3.37 4.03 [a] 3.62 [b]
$ScHI_2$	3.82	2.20	2.99	5.62	5.40	3.13

[a] $*$ MoS_2, [b] $*$ WS_2, and [c] $*$ Phosp.

3.2. Stability

In assessing the stability of the $ScHX_2$ monolayers, the first step involves evaluating their thermodynamic stability by calculating cohesive energies ($E_{cohesive}$) using the following formula [33]:

$$E_{cohesive} = \frac{E_{ScHX2} - E_{Sc} - E_H - E_X}{N} \quad (1)$$

where E_{ScHX2}, is the total energy of the monolayer, E_{Sc} is the total energy of a single Sc atom, E_H is the total energy of a single H atom, E_X is the total energy of the X: Br/I atoms, and N is the number of atoms in the unit cell.

The calculated cohesive energies of $ScHBr_2$ and $ScHI_2$ monolayers are -3.43 and -3.10 eV/atom, respectively. By comparing the calculated cohesive energies with those of the synthesized 2D materials such as phosphorene (-3.44 eV/atom) [34], silicene (-3.94 eV/atom) [35], Be_2C monolayer (-4.84 eV/atom) [36], it is evident that the $ScHX_2$ monolayer (X: Br/I) demonstrates robust structural stability.

Next, to analyze the lattice dynamic stability, we have performed calculations for the phonon band dispersion using Density Functional Perturbation Theory (DFPT), as illustrated in Figure 3. The absence of negative modes in the phonon branches for both monolayers across the entire Brillouin zone confirms the dynamic stability of both monolayers. Due to the increase in the atomic mass from Br to I, the optical phonon branches shift downwards by 5 THz, as expected (Figure 3).

The Born Huang stability criteria have been taken into consideration to investigate the mechanical stability [37].

It includes conditions for a hexagonal system as: $C_{11} > |C_{12}|$, $C_{22} > 0$, $C_{66} > 0$, and $C_{11}C_{22} - C_{12}^2 > 0$. Using the finite difference method [38], the calculated elastic constants, which are listed in Table 2, satisfy the Born Huang Stability criteria. In addition, Ab-initio molecular dynamic simulations (AIMD) by using the canonical NVT ensemble have been carried out to verify the thermal stability at 300 K. The simulations were carried out for 10 ps with a time step of 1 fs using a 4 × 4 periodic supercell. As shown in Figure A4, the total energy fluctuation within the simulation time is very negligible, thereby confirming the thermal stability of the $ScHBr_2$ monolayer.

Table 2. The calculated elastic constants for the $ScHX_2$ monolayers in GPa.

Monolayer	$C_{11} = C_{22}$	C_{12}	C_{66}
$ScHBr_2$	29.95	8.07	10.94
$ScHI_2$	25.07	7.57	8.75

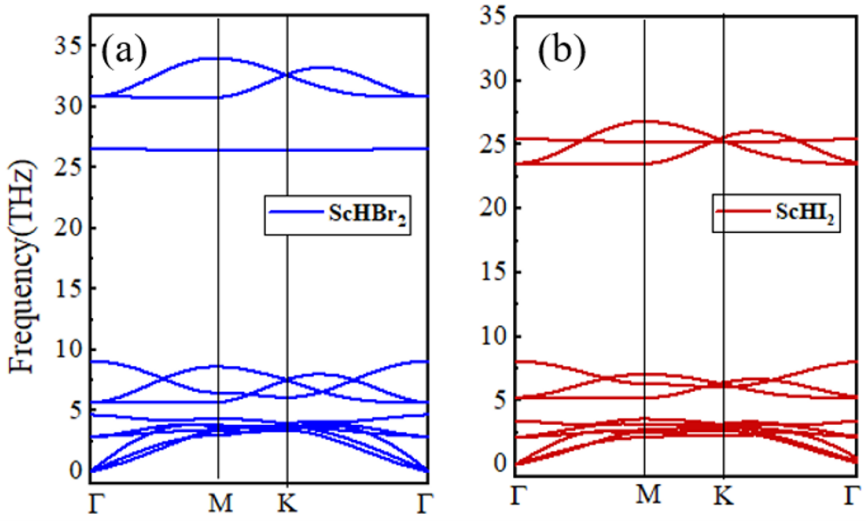

Figure 3. The phonon band structure of (**a**) $ScHBr_2$ and (**b**) $ScHI_2$ monolayer.

3.3. Mechanical Properties

Young's modulus is a measure of a material's stiffness. For materials with a higher Young's modulus, it means that they require a greater amount of stress to induce a given amount of deformation or strain in their structure. In simple terms, they are less prone to deformation and can withstand more stress before changing shape significantly. This property is desirable in applications where structural integrity and resistance to deformation are crucial. Conversely, materials with a lower Young's modulus are more flexible and deform more readily under stress. This characteristic can be advantageous when applying strain to induce electric polarization. In such cases, materials with lower Young's modulus are preferred because they respond more readily to strain-induced changes and can exhibit tailored electronic properties.

The 2D Young's modulus of elasticity (Y_{2D}) and Poisson's ratio (v_{2D}) have been determined using the following.

$$Y_{2D} = \frac{C_{11}^2 - C_{12}^2}{C_{11}}, \qquad v_{2D} = \frac{C_{12}}{C_{11}} \tag{2}$$

Young's modulus and Poisson ratio for the $ScHBr_2$ ($ScHI_2$) monolayer were found to be 27.77 (22.78) GPa and 0.26 (0.30), respectively. The Poisson ratio is less than 0.5 in both of the monolayers as the materials tend to become in-compressible for $v_{2D} > 0.5$. Also, the elastic constants for both the monolayers are in the range of the elastic constants reported for experimentally and theoretically predicted 2D monolayers (MoS_2: 130 N/m (expt), WS_2: 177 N/m (expt), Bi: 25.28 N/m (DFT), $CdCl_2$: 30.0 N/m, (DFT)) [39].

To obtain the orientation angle-dependent Young's modulus $Y(\theta)$ and Poisson's ratio $v(\theta)$, we used the formulation [40,41]:

$$Y(\theta) = \frac{C_{11}C_{22} - C_{12}^2}{C_{11}\sin^4(\theta) + C_{22}\cos^4(\theta) + (C_{11}C_{22} - C_{12}^2)\cos^2(\theta)\sin^2(\theta)} \tag{3}$$

and

$$v(\theta) = \frac{C_{12}(\sin^4(\theta) + \cos^4(\theta)) - (C_{11} + C_{22} - \frac{C_{11}C_{22} - C_{12}^2}{C_{66}})\cos^2(\theta)\sin^2(\theta)}{C_{11}\sin^4(\theta) + C_{22}\cos^4(\theta) + (C_{11}C_{22} - C_{12}^2)\cos^2(\theta)\sin^2(\theta)} \tag{4}$$

From Figure 4, we can observe that, for the $ScHBr_2$ monolayer, Young's modulus, and Poisson ratio values are constant with varying θ, suggesting a negligible degree of anisotropy due to the absence of any deviation from the perfect circle. Thus, the monolayers exhibit mechanical isotropy, i.e., the Young's modulus as well as the Poisson ratio, are

orientation-independent. Similar variation has also been predicted in the $ScHI_2$ monolayer in Figure A5.

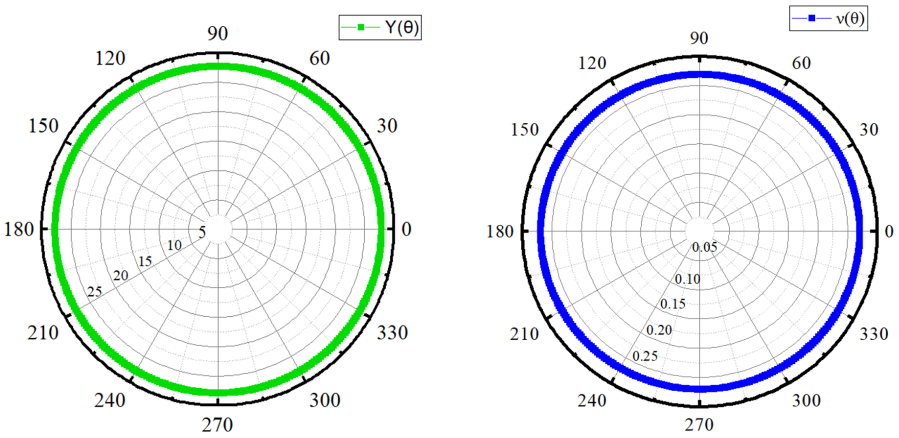

Figure 4. The calculated orientation dependence of Young's modulus (GPa) $Y(\theta)$ and Poisson's ratio $v(\theta)$ for the $ScHBr_2$ monolayer.

3.4. Optical Properties

The optical properties of the monolayers can be obtained using the frequency-dependent dielectric function denoted as $\varepsilon(\omega)$, which represents the linear response of a system to the electromagnetic field. Its real ($\varepsilon_1(\omega)$) and imaginary ($\varepsilon_2(\omega)$) parts can be obtained using the Kramers-Kronig relations [42] and the absorption coefficient (α) is related to $\varepsilon(\omega)$ as follows:

$$\alpha(\omega) = \frac{\omega}{c}\sqrt{2\sqrt{\varepsilon_1^2(\omega) + \varepsilon_2^2(\omega)} - \varepsilon_1(\omega)} \quad (5)$$

where $\varepsilon_1(\omega)$ and $\varepsilon_2(\omega)$ are the real and imaginary parts of the frequency-dependent dielectric function, respectively.

Figure 5 shows the absorbance for the $ScHX_2$ monolayers in the UV-VIS region. The $ScHI_2$ monolayer shows a much higher absorption than the $ScHBr_2$ monolayer. We would like to mention that the G0W0+BSE method provides a better description of the optical properties, as widely observed in the literature [43–45]. However, due to the computational intensiveness of this method, we were unable to employ it in the present study.

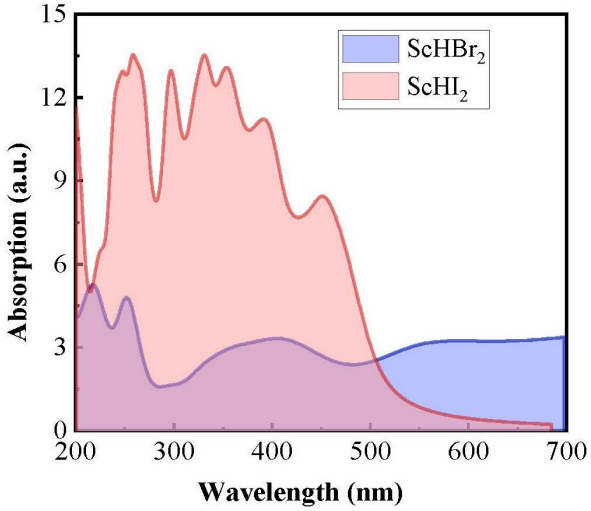

Figure 5. The absorption coefficient of $ScHX_2$ monolayers in UV-VIS wavelength region.

3.5. Strain Engineering

3.5.1. Strain-Induced Modulation in Band Gap

Theoretical and experimental work has demonstrated that strain can play a significant role in manipulating the electronic, mechanical, and optical properties of bulk as well as 2D materials. However, traditional semiconductor bulk single crystals can only endure very limited strain, significantly constraining the application of strain modulation. In contrast, two-dimensional (2D) materials exhibit a much higher capacity for deformation and can withstand greater elastic strain without fracturing, making them highly promising candidates for strain engineering [46–51]. However, in experimental studies, the strain within the material may not be uniform, making it challenging to accurately evaluate atomic bond lengths and internal strain, especially on a statistical basis using large samples. To address this complexity, two primary methods are frequently employed to measure strain: local strain measurement and global strain measurement. Local strain measurement focuses on individual atomic bonds and their immediate environment, often using microscopic visual techniques such as transmission electron microscopy (TEM) or atomic force microscopy (AFM) to provide high-resolution images of the strained regions. On the other hand, global strain measurement evaluates the overall deformation of the material and often utilizes spectral measurement techniques like Raman spectroscopy or X-ray diffraction (XRD) to assess strain across a larger sample [47].

The strain-induced changes in bond length are directly correlated with changes in the energy within a material. When strain is applied, the atomic bonds can either stretch or compress, leading to variations in the total energy of the system (Figure A6). This relationship between bond length and energy is crucial for understanding how materials respond to mechanical deformation and for predicting their mechanical and electronic properties under different strain conditions.

On the application of the biaxial tensile strain, the bandgap reduces to 2.29 eV and 1.80 eV for $ScHBr_2$ and $ScHI_2$ respectively. However, with the application of the biaxial compressive strain, the band gap decreases from 2.49 to 1.37 eV for the $ScHI_2$ monolayer and for the $ScHBr_2$ monolayer, the band gap increases from 2.98 eV to 3.13 eV up to 5% biaxial compressive strain but then decreases as we go beyond 5% to 2.62 eV (Figure 6). To gain a deeper understanding of this change in trend, we have computed the orbital decomposed band structure at each strain value for the $ScHBr_2$ monolayer, as illustrated in Figure 7. We can observe that with increasing the compressive strain, the lower valence bands shift towards the Fermi level (E = 0), leading VBM shift from the k point (Γ-M) to Γ. Moreover, we noticed a significant change in the band composition going from 5% to 6% biaxial compressive strain. At the 5% compressive strain, 61% contribution comes from the Br-*p* and 24% H-*s* orbitals at VBM. In contrast, at the 6% compressive strain, VBM shifts to Γ point with 80% contribution from the Br-*px* orbitals. Additionally, with the increase in the biaxial tensile strain, CBM composed of the Sc-*d* orbitals shifts towards the Fermi level, thereby lowering the band gap of the monolayer.

Also to confirm the stability of the strained monolayer we have also investigated the phonon bandstructure at 5% tensile as well as compressive strain (Figure A7). The absence of any significant negative phonon bands confirmed the dynamical stability of the strained monolayer.

For the $ScHI_2$ monolayer, the variation in the orbital decomposed band structures has been displayed in Figure 8.

Application of the biaxial strain reduces the band gap to 1.76 eV for the (7%) compressive and 2.00 eV for the (7%) tensile strain (Figure 8). In the case of biaxial tensile strain, CBM shifts to the Γ (strain $>$ 1%), with lowering the CBM close to the Fermi level which reduces the bandgap and VBM remains the same (Γ-M) (Figure 8). On the other hand, for the compressive strain, VBM shifts to Γ (strain $>$ 1%), moving the CBM towards the Fermi level at the same k point.

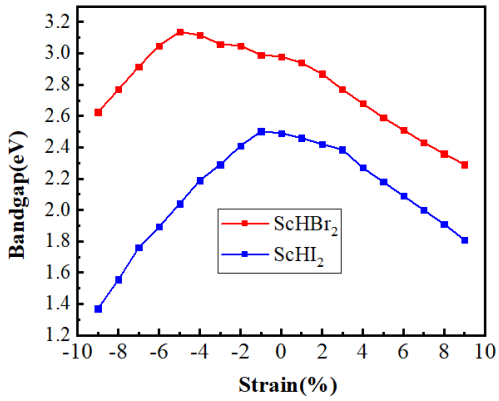

Figure 6. The calculated variation of the band gap in $ScHX_2$ monolayers with tensile and compressive biaxial strain.

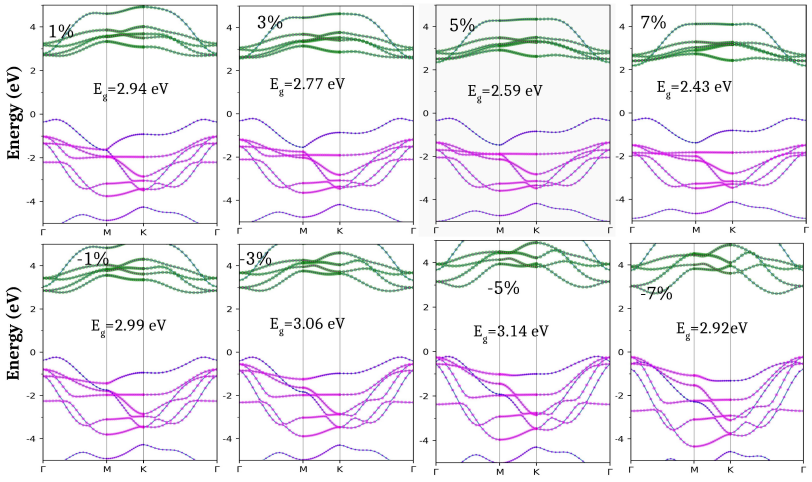

Figure 7. Atomic Orbital-projected band structure for $ScHBr_2$ monolayer under the application of tensile and compressive biaxial strain using GGA-PBE. Color Code; Sc-*s*: yellow, Sc-*p*: brown, Sc-*d*: green, H-*s*: blue, I-*s*: cyan, I-*p*: pink and I-*d*: orange.

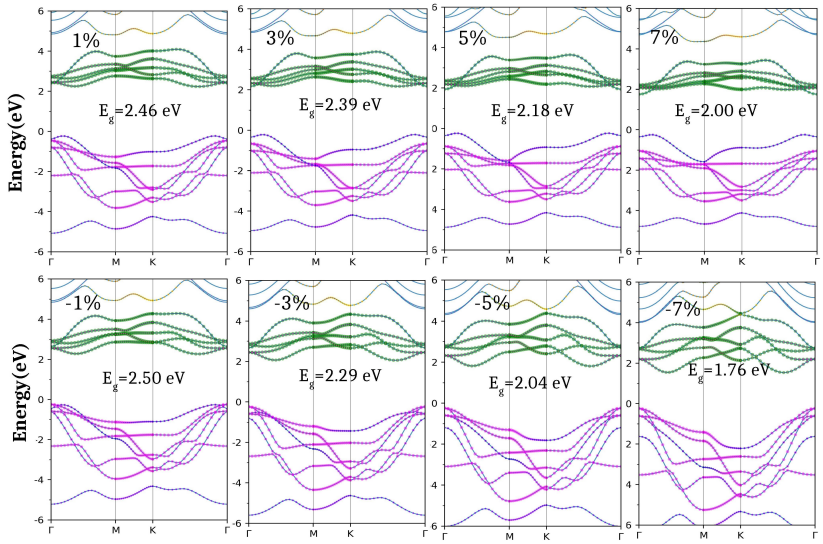

Figure 8. Atomic Orbital-projected band structure for $ScHI_2$ monolayer under the application of tensile and compressive biaxial strain using GGA-PBE. Color Code; Sc-*s*: yellow, Sc-*p*: brown, Sc-*d*: green, H-*s*: blue, I-*s*: cyan, -*p*: pink and I-*d*: orange.

To investigate the application of strain-engineering in the field of water-splitting we have compared the band edges to the oxidation and reduction potentials of water. Figure 9 depicts the alignment of VBM and CBM relative to the water redox potentials. A detailed discussion has been provided in the Appendix A. The results indicate the suitability of the energies of the band edges of the $ScHBr_2$ monolayer for O_2 and H_2 evolution. However this is not the case for the $ScHI_2$ monolayer, for which CBM does straddle the reduction potential but VBM doesn't straddle the oxidation potential, as shown in Figure A8.

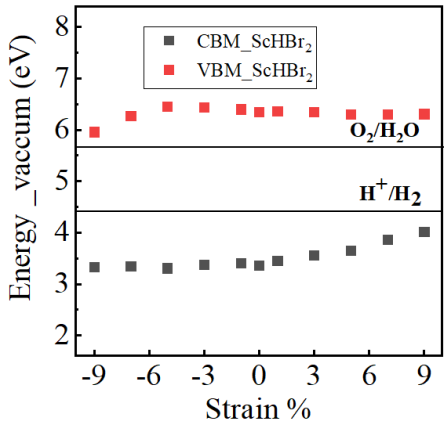

Figure 9. The calculated strain-induced variation in VBM and CBM positions with respect to the redox potential for the $ScHBr_2$ monolayer.

3.5.2. Strain-Induced Modulations in Effective Masses

The effective mass of the charge carriers is a crucial parameter for devices as it plays a significant role in determining their transport properties and optical performance. It is determined by approximating the second derivatives of the VBM and CBM concerning the wave vector k and can be expressed as:

$$\frac{1}{m^*} = \frac{1}{\hbar^2}\left(\frac{d^2E}{dk^2}\right) \quad (6)$$

A flat band suggests the presence of heavy carriers or a high effective mass, whereas the well-dispersed bands indicate light carriers or a low effective mass. The strain affects the dispersion of the bands, reflected in a change in the effective masses of electrons and holes. Hence, the effective mass of electrons (holes) is determined by the dispersion of the energy bands at the CBM (VBM).

The effective masses for electrons and holes for both the monolayers for several strain values have been provided in Table 3. The effective mass is directly related to the carrier mobility, implying that the hole mobility in $ScHX_2$ monolayers is predicted to be higher than that of electrons in the pristine $ScHX_2$ monolayer.

In the case of the $ScHBr_2$ monolayer, we can observe that the effective masses of the hole for the tensile as well as compressive strain remain almost similar since the curvature/dispersion of the bands remains nearly the same. However, a strain-induced range of variation is observed for the electron-effective masses. This variation is attributed to the change in the positions of the CBM as can also be observed from the orbital decomposed band structure in Figure 7. We can observe that for the tensile strain, the upper conduction band shifts towards the Fermi level. Hence the CBM now shifts to Γ for strain $> 1\%$. It lowers the effective masses of electrons from 2.38 m_0 to 0.83 m_0 since now the conduction band has more dispersion at CBM. Whereas no shifting of the CBM is observed in the case of compressive strain hence the electron effective masses almost remain the same.

Table 3. Electron and Hole Effective Masses for pristine and strained $ScHX_2$ monolayer.

Strain	%	$ScHBr_2$		$ScHI_2$	
		Electron	Hole	Electron	Hole
Compressive	7%	1.09	−1.05	0.77	−1.09
Compressive	5%	1.48	−0.63	0.91	−1.32
Compressive	3%	1.58	−0.65	1.11	−1.52
Compressive	1%	1.67	−0.77	1.45	−1.68
Pristine	0%	2.87	−0.98	1.57	−0.51
Tensile	1%	2.38	−0.65	1.94	−0.53
Tensile	3%	0.95	−0.72	2.66	−0.61
Tensile	5%	0.65	−0.76	0.44	−0.69
Tensile	7%	0.83	−0.86	0.48	−0.78

In contrast, for the case of the $ScHI_2$ monolayer, Table 3 shows similar behavior for the biaxial tensile strain since the hole effective mass remains nearly the same. However, the hole becomes heavier with the tensile strain as the valance band becomes flatter at VBM (Figure 8). In contrast, for the case of the compressive strain, VBM shifts towards Γ leading to a decrease in the hole's effective mass. A subsequent increase in the compressive strain leads to a decrease in the hole effective mass from 1.68 m_0 to 1.09 m_0 due to an increase in the dispersion of the valence band at VBM. Also, the application of the compressive strain makes the electron lighter hence the effective mass reduces to 0.77 m_0 (7%). Whereas in the case of tensile strain, CBM remains almost flat at 3%, which increases the electron effective mass to 2.66 m_0. A further increase in the tensile strain shifts CBM towards Γ, lowering the electron effective mass to 0.48 m_0 (Table 3).

3.6. Substrate Supported $ScHBr_2$ Monolayer

In general, the fabrication of an electronic device requires a substrate that is expected to be weakly bonded to the material. The choice of substrates is governed by lattice mismatch between the two, though the dry transfer method can be used for the large mismatched materials. In this study, our choice of substrate is a hexagonal 2D GaN monolayer as a substrate, which has been experimentally synthesized and theoretically studied [52–54]. Figure 10a displays the configuration of $ScHBr_2$/GaN heterostructure for which the lattice mismatch is calculated to be 11.6%. The inter-layer distance is 3.46 Å and the bandgap is 1.89 eV as shown in Figure 10b. The strained $ScHBr_2$ monolayer dominates the CBM and GaN denominates the VBM of the heterostructure hence forming a Type-II heterostructure.

The degree of interaction between the substrate and the monolayer can be quantified as follows:

$$E_{\text{interaction}} = E_{\text{heterostructure}} - E_{\text{GaN}} - E_{\text{monolayer}} \quad (7)$$

where $E_{\text{heterostructure}}$, $E_{\text{monolayer}}$, and E_{GaN} are the energies of the interface, monolayer, and the GaN substrate. The interaction energy was calculated to be −0.079 eV therefore indicating the feasibility of the formation of the heterostructure due to Equation (7) being exothermic. The interaction is mainly attributed to a charge transfer of 0.03 e from the monolayer to the substrate, as per Bader charge analysis. This is further confirmed by the charge density difference. The charge density difference calculated using Equation 8 also confirms a small charge transfer at the interface (Figure 11a)

$$\rho_r = \rho_{\text{interface}} - (\rho_{\text{substrate}} - \rho_{\text{monolayer}}) \quad (8)$$

The charge transfer is expected to induce a large intrinsic electric field across the interface which is displayed in Figure 11b with ΔU = 8.61 eV. Overall the substrate-induced modifications in the $ScHBr_2$ monolayer appear minimal retaining the semiconducting nature of the monolayer. Note that the calculated interaction energy of $ScHBr_2$ with the most commonly used graphene is predicted to be endothermic, thereby making the formation of the $ScHBr_2$/graphene heterostructure challenging.

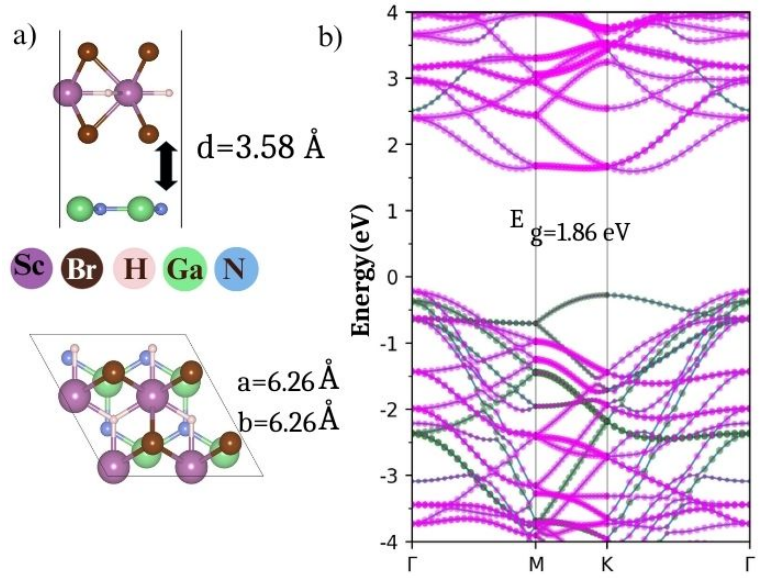

Figure 10. (**a**) Side and top views (**b**) band structure of the $ScHBr_2$/GaN heterostructure where the bands contributed by the $ScHBr_2$ monolayer are indicated by magenta color and bands contributed by GaN are indicated by emerald color.

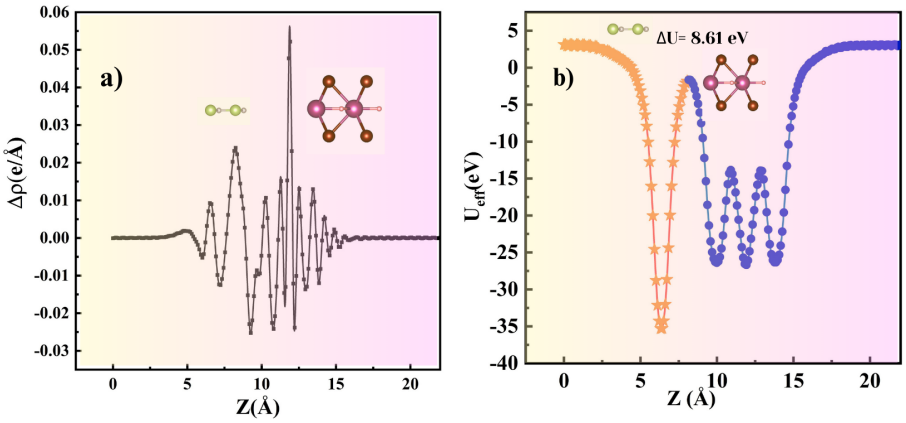

Figure 11. (**a**) Plane-averaged differential charge density ($\Delta\rho$) (**b**) Plane-averaged electrostatic effective potential (U_{eff}) along the z direction of the heterostructure.

4. Conclusions

In this study, novel mixed anion two-dimensional materials, $ScHX_2$ (where X: Br/I), are investigated employing the density functional theory (DFT). Our findings indicate that the monolayers are stable according to various well-established parameters. It's noteworthy that the electronic properties of these $ScHX_2$ monolayers are comparable to well-established 2D materials like graphene and MoS_2, making them highly suitable for electronic devices. Furthermore, we have comprehensively explored the mechanical, optical, and photocatalytic properties and have systematically compared them with the existing monolayers. Our investigation also delved into the influence of strain on charge carrier masses, offering insights into the potential mobility of charge carriers under varying strain conditions. The substrate-induced modification in the structural and electronic properties of the $ScHBr_2$ monolayer appears minimal retaining the semiconducting nature of the monolayer.

Author Contributions: Conceptualization, A.R.; methodology, A.R.; writing—original draft preparation, A.R.; writing—review and editing, R.P.; visualization, A.R.; funding acquisition, R.P. All authors have read and agreed to the published version of the manuscript.

Funding: This research received no external funding.

Data Availability Statement: The data is available in the Appendix A.

Acknowledgments: The authors would like to thank the computational facilities provided by Michigan Technological University.

Conflicts of Interest: The authors declare no conflicts of interest.

Appendix A

The orientation angle-dependent Young's modulus (θ) and Poisson's ratio $v(\theta)$ for the SHI_2 monolayer have been described in Figure A5. The plot for the $ScHI_2$ monolayer is similar to the $ScHBr_2$ monolayer with Young's modulus of 22.78 GPa and Poisson ratio of 0.30.

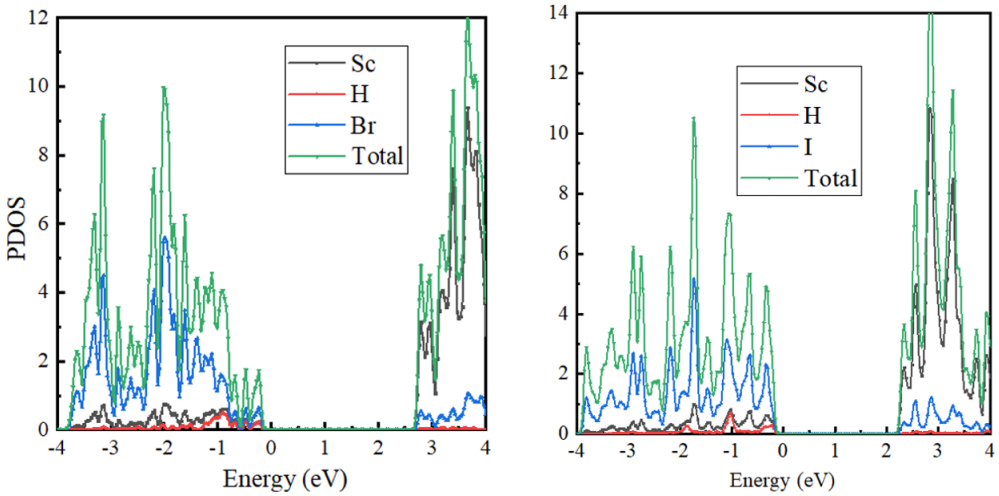

Figure A1. Partial Density of States (PDOS) of the $ScHX_2$ monolayers.

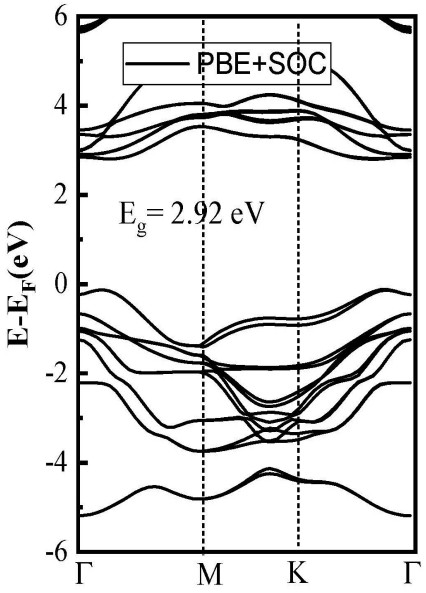

Figure A2. PBE + SOC bandstructure of the $ScHBr_2$ monolayer.

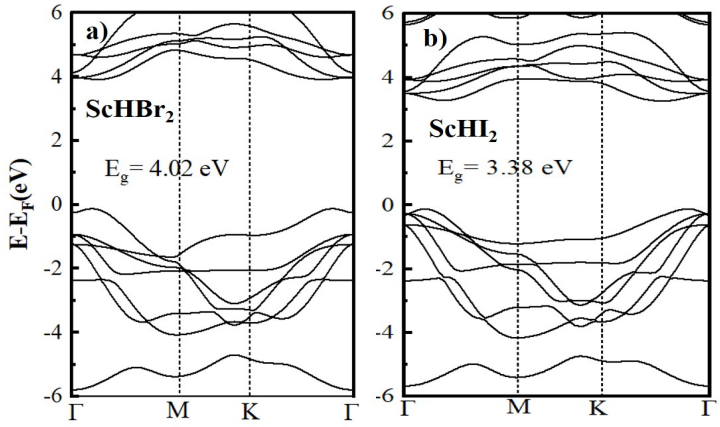

Figure A3. HSE06 bandstructures of (**a**) $ScHBr_2$ (**b**) $ScHI_2$ monolayers.

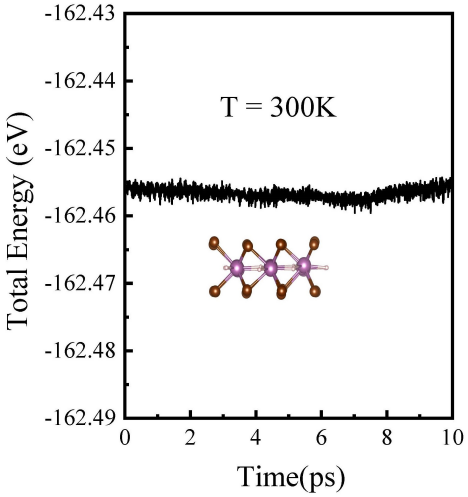

Figure A4. Fluctuations in Total Energy at 300 K for 10 ps of $ScHBr_2$ monolayer.

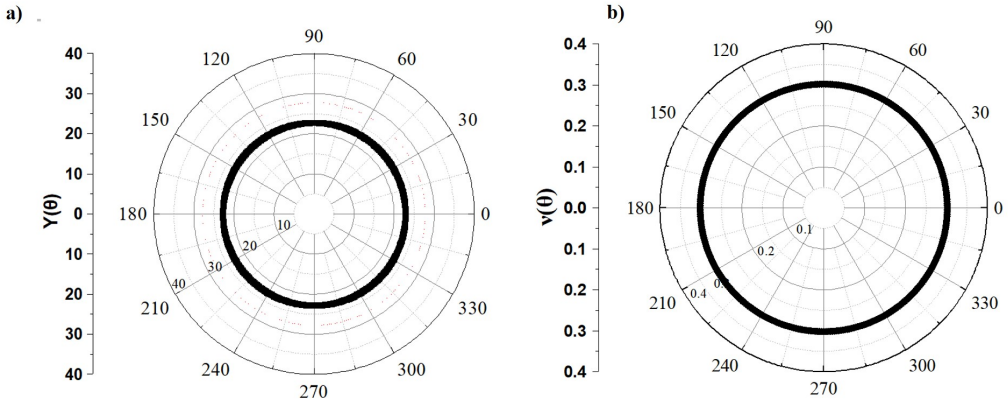

Figure A5. Orientation dependent (**a**) Young's modulus, $Y(\theta)$ (GPa) and (**b**) Poisson's ratio, $v(\theta)$ of $ScHI_2$ monolayer.

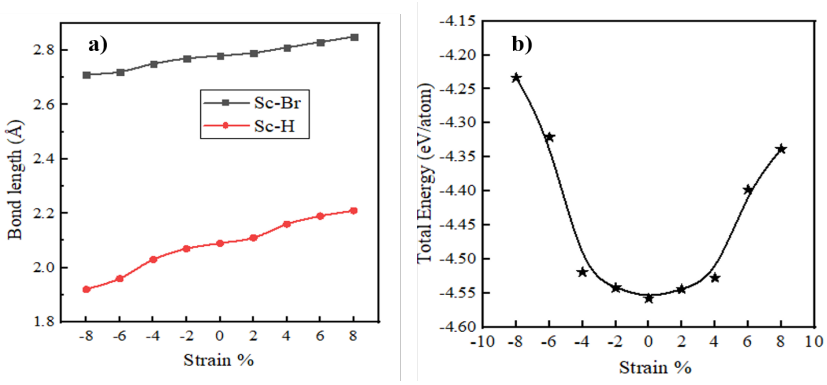

Figure A6. Variation in (**a**) Bond−Lengths (**b**) Total Energy (eV/atom) of the $ScHBr_2$ monolayer with strain.

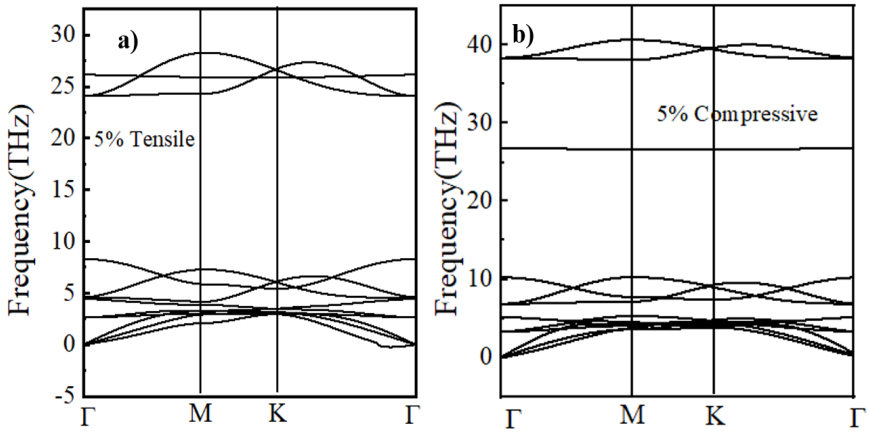

Figure A7. Phonon Bandstructure of 5% (**a**) Tensile and (**b**) Compressive strained $ScHBr_2$ monolayer.

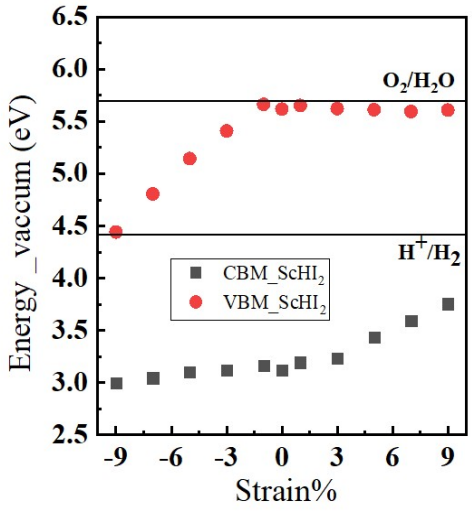

Figure A8. Variation in the positions of the VBM and CBM with respect to the redox potentials for the $ScHI_2$ monolayer with strain.

For water splitting, the material needs to have a minimum band gap (E_g) of 1.23 eV to absorb incident photons with energy $E \geq 1.23$ eV, corresponding to a wavelength $\lambda \leq 1010$ nm under standard conditions ($T = 298$ K, $P = 1$ bar, and pH $= 0$). Furthermore, it must have suitable band edges that straddle the redox potentials of water to drive the kinetics of the hydrogen evolution (reduction) and oxygen evolution (oxidation) reactions (HER and OER reactions). On the absolute vacuum scale at pH $= 0$, a band gap of 1.23 eV

corresponds to a conduction band minimum (CBM) ideally situated at −4.44 eV, which is the reduction potential for HER (H^+/H_2), and a valence band maximum (VBM) at −5.67 eV, which is the oxidation potential for OER (H_2O/O_2). If the energy levels of the CBM and VBM are positive and negative relative to the reduction and oxidation potentials, respectively, the water-splitting reaction will be thermodynamically favored.

Since strain influences the curvature of the electronic bands, it can cause shifts in the energy levels of CBM and VBM, thereby modifying alignments of CBM/VBM relative to the redox potentials of water under strain. To assess the thermodynamic feasibility of HER/OER, it is essential to verify that the band edges under strain continue to straddle the redox potentials of water. Hence, any analysis of strain effects on 2D materials or other semiconductors must include a thorough evaluation of how strain impacts the positioning of CBM and VBM concerning the redox potentials to ensure continued photocatalytic activity. From Figure 9, we can observe that the energy difference between the H^+/H_2 potential and the CBM which can be referred to as CBO (conduction band offset), and the energy difference between the O_2/H_2O potential and the VBM referred to as VBO vary with the application of strain. As biaxial compressive strain is applied, the energy difference between the H^+/H_2 potential and the CBM (CBO) is raised, increasing the thermodynamic driving force of the excited electrons to participate in HER, whereas as the energy difference between the O_2/H_2O potential and the VBM (VBO) decreases, as listed in Table A1. For the biaxial tensile strain, both the CBO and VBO reduce compared to the unstrained monolayer. Hence there will be selective enhancement of HER over OER due to compressive strain [55].

Table A1. Variation in energy difference between the H^+/H_2 (O_2/H_2O) potential and CBM (VBM) as CBO (VBO) with strain for $ScHBr_2$ monolayer.

Strain %	CBO (eV)	VBO (eV)
−9%	1.11	0.29
−7%	1.11	0.59
−5%	1.13	0.78
−3%	1.06	0.77
−1%	1.03	0.73
0	1.07	0.67
1%	0.98	0.70
3%	0.87	0.68
5%	0.78	0.64
7%	0.57	0.63
9%	0.42	0.64

Graphene/$ScHBr_2$ Hetero-structure: The binding energy for the graphene/$ScHBr_2$ hetero-structure was found to be 10 meV which indicated the unlikely synthesis of the $ScHBr_2$ monolayer on the graphene as a substrate.

POSCAR

```
Sc1 H1 Br2
1.0
        3.6170041561          0.0000000000          0.0000000000
       -1.8085020781          3.1324174848          0.0000000000
        0.0000000000          0.0000000000         24.4537048340
   Sc    H   Br
    1    1    2
Cartesian
```

```
     0.000000000         0.000000000        15.894907559
     0.000000000         2.088278385        15.894907559
     1.808502132         1.044139193        14.048772084
     1.808502132         1.044139193        17.741044492

Sc1 H1 I2
1.0
       3.8151557446         0.0000000000         0.0000000000
      -1.9075778723         3.3040217942         0.0000000000
       0.0000000000         0.0000000000        25.8316631317
   Sc    H    I
    1    1    2
Cartesian
     0.000000000         0.000000000        16.790580420
     0.000000000         2.202681262        16.790580420
     1.907577929         1.101340631        14.768290709
     1.907577929         1.101340631        18.812871670
```

References

1. Kageyama, H.; Hayashi, K.; Maeda, K.; Attfield, J.P.; Hiroi, Z.; Rondinelli, J.M.; Poeppelmeier, K.R. Expanding frontiers in materials chemistry and physics with multiple anions. *Nat. Commun.* **2018**, *9*, 772. [CrossRef] [PubMed]
2. Hitoki, G.; Takata, T.; Kondo, J.N.; Hara, M.; Kobayashi, H.; Domen, K. An oxynitride, TaON, as an efficient water oxidation photocatalyst under visible light irradiation ($\lambda \geq 500$ nm). *Chem. Commun.* **2002**, *16*, 1698–1699. [CrossRef]
3. Maeda, K.; Takata, T.; Hara, M.; Saito, N.; Inoue, Y.; Kobayashi, H.; Domen, K. GaN: ZnO solid solution as a photocatalyst for visible-light-driven overall water splitting. *J. Am. Chem. Soc.* **2005**, *127*, 8286–8287. [CrossRef] [PubMed]
4. Fujito, H.; Kunioku, H.; Kato, D.; Suzuki, H.; Higashi, M.; Kageyama, H.; Abe, R. Layered perovskite oxychloride Bi4NbO8Cl: A stable visible light responsive photocatalyst for water splitting. *J. Am. Chem. Soc.* **2016**, *138*, 2082–2085. [CrossRef]
5. Kobayashi, G.; Hinuma, Y.; Matsuoka, S.; Watanabe, A.; Iqbal, M.; Hirayama, M.; Yonemura, M.; Kamiyama, T.; Tanaka, I.; Kanno, R. Pure H–conduction in oxyhydrides. *Science* **2016**, *351*, 1314–1317. [CrossRef]
6. Imanaka, N.; Misran, M.R.I.B.; Nunotani, N. Evidence for enormous iodide anion migration in lanthanum oxyiodide–based solid. *Sci. Adv.* **2021**, *7*, eabh0812. [CrossRef]
7. Zhao, L.D.; He, J.; Berardan, D.; Lin, Y.; Li, J.F.; Nan, C.W.; Dragoe, N. BiCuSeO oxyselenides: New promising thermoelectric materials. *Energy Environ. Sci.* **2014**, *7*, 2900–2924. [CrossRef]
8. Mizuguchi, Y. Material development and physical properties of BiS2-based layered compounds. *J. Phys. Soc. Jpn.* **2019**, *88*, 041001. [CrossRef]
9. Kraft, M.A.; Culver, S.P.; Calderon, M.; Böcher, F.; Krauskopf, T.; Senyshyn, A.; Dietrich, C.; Zevalkink, A.; Janek, J.; Zeier, W.G. Influence of lattice polarizability on the ionic conductivity in the lithium superionic argyrodites Li6PS5X (X = Cl, Br, I). *J. Am. Chem. Soc.* **2017**, *139*, 10909–10918. [CrossRef]
10. Kamaya, N.; Homma, K.; Yamakawa, Y.; Hirayama, M.; Kanno, R.; Yonemura, M.; Kamiyama, T.; Kato, Y.; Hama, S.; Kawamoto, K.; et al. A lithium superionic conductor. *Nat. Mater.* **2011**, *10*, 682–686. [CrossRef]
11. Hu, Y.; Wu, X.; Ortiz, B.R.; Ju, S.; Han, X.; Ma, J.; Plumb, N.C.; Radovic, M.; Thomale, R.; Wilson, S.D.; et al. Rich nature of Van Hove singularities in Kagome superconductor CsV3Sb5. *Nat. Commun.* **2022**, *13*, 2220. [CrossRef] [PubMed]
12. Li, J.; Yu, Q.; He, Y.; Stoumpos, C.C.; Niu, G.; Trimarchi, G.G.; Guo, H.; Dong, G.; Wang, D.; Wang, L.; et al. Cs2PbI2Cl2, all-inorganic two-dimensional Ruddlesden–Popper mixed halide perovskite with optoelectronic response. *J. Am. Chem. Soc.* **2018**, *140*, 11085–11090. [CrossRef]
13. Mounet, N.; Gibertini, M.; Schwaller, P.; Campi, D.; Merkys, A.; Marrazzo, A.; Sohier, T.; Castelli, I.E.; Cepellotti, A.; Pizzi, G.; et al. Two-dimensional materials from high-throughput computational exfoliation of experimentally known compounds. *Nat. Nanotechnol.* **2018**, *13*, 246–252. [CrossRef] [PubMed]
14. Hvazdouski, D.C.; Baranava, M.S.; Korznikova, E.A.; Kistanov, A.A.; Stempitsky, V.R. Search on stable binary and ternary compounds of two-dimensional transition metal halides. *2D Mater.* **2024**, *11*, 025022. [CrossRef]
15. Haastrup, S.; Strange, M.; Pandey, M.; Deilmann, T.; Schmidt, P.S.; Hinsche, N.F.; Gjerding, M.N.; Torelli, D.; Larsen, P.M.; Riis-Jensen, A.C.; et al. The Computational 2D Materials Database: High-throughput modeling and discovery of atomically thin crystals. *2D Mater.* **2018**, *5*, 042002. [CrossRef]
16. Olsen, T.; Andersen, E.; Okugawa, T.; Torelli, D.; Deilmann, T.; Thygesen, K.S. Discovering two-dimensional topological insulators from high-throughput computations. *Phys. Rev. Mater.* **2019**, *3*, 024005. [CrossRef]
17. Michaelis, C.; Mattausch, H.; Borromann, H.; Simon, A.; Cockroft, J. LnHal2Hn Neue Phasen in den ternären Systemen Ln/Hal/HI Strukturen. *Z. Anorg. Allg. Chem.* **1992**, *607*, 29–33. [CrossRef]

18. Li, M.; Ford, M.J.; Kobayashi, R.; Amos, R.D.; Reimers, J.R. Reliable density functional and G_0 W_0 approaches to the calculation of bandgaps in 2D materials. *arXiv* **2023**. [CrossRef]
19. Kresse, G.; Furthmüller, J. Efficient iterative schemes for ab initio total-energy calculations using a plane-wave basis set. *Phys. Rev. B* **1996**, *54*, 11169. [CrossRef]
20. Kresse, G.; Hafner, J. Ab initio molecular dynamics for liquid metals. *Phys. Rev. B* **1993**, *47*, 558. [CrossRef]
21. Kresse, G.; Furthmüller, J. Efficiency of ab-initio total energy calculations for metals and semiconductors using a plane-wave basis set. *Comput. Mater. Sci.* **1996**, *6*, 15–50. [CrossRef]
22. Kresse, G.; Hafner, J. Ab initio molecular-dynamics simulation of the liquid-metal–amorphous-semiconductor transition in germanium. *Phys. Rev. B* **1994**, *49*, 14251. [CrossRef] [PubMed]
23. Perdew, J.P.; Burke, K.; Ernzerhof, M. Generalized gradient approximation made simple. *Phys. Rev. Lett.* **1996**, *77*, 3865. [CrossRef]
24. Grimme, S.; Antony, J.; Ehrlich, S.; Krieg, H. A consistent and accurate ab initio parametrization of density functional dispersion correction (DFT-D) for the 94 elements H-Pu. *J. Chem. Phys.* **2010**, *132*, 154104. [CrossRef] [PubMed]
25. Baroni, S.; De Gironcoli, S.; Dal Corso, A.; Giannozzi, P. Phonons and related crystal properties from density-functional perturbation theory. *Rev. Mod. Phys* **2001**, *73*, 515. [CrossRef]
26. Togo, A.; Oba, F.; Tanaka, I. First-principles calculations of the ferroelastic transition between rutile-type and $CaCl_2$-type SiO_2 at high pressures. *Phys. Rev. B* **2008**, *78*, 134106. [CrossRef]
27. Togo, A.; Tanaka, I. First principles phonon calculations in materials science. *Scripta Mater.* **2015**, *108*, 1–5. [CrossRef]
28. Kim, H.G.; Choi, H.J. Thickness dependence of work function, ionization energy, and electron affinity of Mo and W dichalcogenides from DFT and GW calculations. *Phys. Rev. B* **2021**, *103*, 085404. [CrossRef]
29. Sun, H.; Shang, Y.; Yang, Y.; Guo, M. Realization of N-type semiconducting of phosphorene through surface metal doping and work function study. *J. Nanomater.* **2018**, *2018*, 1–9. [CrossRef]
30. Liu, Y.; Stradins, P.; Wei, S.H. Van der Waals metal-semiconductor junction: Weak Fermi level pinning enables effective tuning of Schottky barrier. *Sci. Adv.* **2016**, *2*, e1600069. [CrossRef]
31. Yang, W.; Xin, K.; Yang, J.; Xu, Q.; Shan, C.; Wei, Z. 2D ultrawide bandgap semiconductors: Odyssey and challenges. *Small Methods* **2022**, *6*, 2101348. [CrossRef]
32. Torelli, D.; Moustafa, H.; Jacobsen, K.W.; Olsen, T. High-throughput computational screening for two-dimensional magnetic materials based on experimental databases of three-dimensional compounds. *Npj Comput. Mater.* **2020**, *6*, 158. [CrossRef]
33. Wang, M.; Han, D. Thermal Properties of 2D Dirac Materials MN4 (M = Be and Mg): A First-Principles Study. *ACS Omega* **2022**, *7*, 10812–10819. [CrossRef] [PubMed]
34. Qin, G.; Yan, Q.B.; Qin, Z.; Yue, S.Y.; Hu, M.; Su, G. Anisotropic intrinsic lattice thermal conductivity of phosphorene from first principles. *Phys. Chem. Chem. Phys.* **2015**, *17*, 4854–4858. [CrossRef]
35. Drummond, N.; Zolyomi, V.; Fal'Ko, V. Electrically tunable band gap in silicene. *Phys. Rev. B* **2012**, *85*, 075423. [CrossRef]
36. Li, Y.; Liao, Y.; Chen, Z. Be2C monolayer with quasi-planar hexacoordinate carbons: A global minimum structure. *Angew. Chem. Int. Ed.* **2014**, *53*, 7248–7252. [CrossRef] [PubMed]
37. Mouhat, F.; Coudert, F.X. Necessary and sufficient elastic stability conditions in various crystal systems. *Phys. Rev. B* **2014**, *90*, 224104. [CrossRef]
38. Kresse, G.; Furthmüller, J.; Hafner, J. Ab initio force constant approach to phonon dispersion relations of diamond and graphite. *Europhys. Lett.* **1995**, *32*, 729. [CrossRef]
39. Choudhary, K.; Cheon, G.; Reed, E.; Tavazza, F. Elastic properties of bulk and low-dimensional materials using van der Waals density functional. *Phys. Rev. B* **2018**, *98*, 014107. [CrossRef]
40. Hung, N.T.; Nugraha, A.R.; Saito, R. Two-dimensional MoS2 electromechanical actuators. *J. Phys. D Appl. Phys.* **2018**, *51*, 075306. [CrossRef]
41. Xiong, W.; Huang, K.; Yuan, S. The mechanical, electronic and optical properties of two-dimensional transition metal chalcogenides MX 2 and M 2 X 3 (M = Ni, Pd; X = S, Se, Te) with hexagonal and orthorhombic structures. *J. Mater. Chem. C* **2019**, *7*, 13518–13525. [CrossRef]
42. Gajdoš, M.; Hummer, K.; Kresse, G.; Furthmüller, J.; Bechstedt, F. Linear optical properties in the projector-augmented wave methodology. *Phys. Rev. B* **2006**, *73*, 045112. [CrossRef]
43. Shu, H.B.; Guo, J.Y. Structural, electronic, and optical properties of C3B and C3B0·5N0.5 monolayers: A many-body study. *Physica E* **2022**, *138*, 115119. [CrossRef]
44. Shu, H. Two Janus Ga2STe monolayers and their electronic, optical, and photocatalytic properties. *Phys. Chem. Chem. Phys.* **2023**, *25*, 7937–7945. [CrossRef] [PubMed]
45. Shu, H.; Guo, J. Enhanced stability and tunable optoelectronic properties of silicon–carbon monolayers by strain and surface functionalization. *J. Mater. Chem. C* **2024**, *12*, 5916–5925. [CrossRef]
46. Shu, H. Strain effects on stability, electronic and optical properties of two-dimensional C4X2 (X = F, Cl, Br). *J. Mater. Chem. C* **2021**, *9*, 4505–4513. [CrossRef]
47. Peng, Z.; Chen, X.; Fan, Y.; Srolovitz, D.J.; Lei, D. Strain engineering of 2D semiconductors and graphene: From strain fields to band-structure tuning and photonic applications. *Light. Sci. Appl.* **2020**, *9*, 190. [CrossRef]
48. Shu, H.; Niu, X.; Ding, X.; Wang, Y. Effects of strain and surface modification on stability, electronic and optical properties of GaN monolayer. *Appl. Surf. Sci.* **2019**, *479*, 475–481. [CrossRef]

49. Shu, H. Adjustable electro-optical properties of novel graphene-like SiC2 via strain engineering. *Appl. Surf. Sci.* **2021**, *559*, 149956. [CrossRef]
50. Caglayan, R.; Guler, H.; Mogulkoc, Y. An analysis of Schottky barrier in silicene/Ga2SeS heterostructures by employing electric field and strain. *Phys. Chem. Chem. Phys.* **2022**, *24*, 10210–10221. [CrossRef]
51. Mogulkoc, Y.; Caglayan, R.; Ciftci, Y. Band Alignment in Monolayer Boron Phosphide with Janus MoSSe Heterobilayers under Strain and Electric Field. *Phys. Rev. Appl.* **2021**, *16*, 024001. [CrossRef]
52. Sahu, T.K.; Sahu, S.P.; Hembram, K.; Lee, J.K.; Biju, V.; Kumar, P. Free-standing 2D gallium nitride for electronic, excitonic, spintronic, piezoelectric, thermoplastic, and 6G wireless communication applications. *NPG Asia Mater.* **2023**, *15*, 49. [CrossRef]
53. Onen, A.; Kecik, D.; Durgun, E.; Ciraci, S. GaN: From three-to two-dimensional single-layer crystal and its multilayer van der Waals solids. *Phys. Rev. B* **2016**, *93*, 085431. [CrossRef]
54. Qin, Z.; Qin, G.; Zuo, X.; Xiong, Z.; Hu, M. Orbitally driven low thermal conductivity of monolayer gallium nitride (GaN) with planar honeycomb structure: A comparative study. *Nanoscale* **2017**, *9*, 4295–4309. [CrossRef] [PubMed]
55. Kraus, A.O.; Portugal, G.R.; Arantes, J.T. Modulation of band alignment with water redox potentials by biaxial strain on orthorhombic $NaTaO_3$ thin films. *Phys. Chem. Chem. Phys.* **2020**, *22*, 23810–23815. [CrossRef] [PubMed]